# Machine Learning-Guided Discovery of $^{19}$F MRI Agents Enabled by Automated Copolymer Synthesis

Marcus Reis[1,†], Filipp Gusev[2,3,†] Nicholas G. Taylor[1,†], Sang Hun Chung[4], Matthew D. Verber,[1] Yueh Z. Lee[5], Olexandr Isayev[2,3*], Frank A. Leibfarth[1,*]

[1]*Department of Chemistry, University of North Carolina at Chapel Hill, Chapel Hill, NC 27599*

[2]*Department of Chemistry, Mellon College of Science, Carnegie Mellon University, Pittsburgh, PA 15213*

[3]*Computational Biology Department, School of Computer Science, Carnegie Mellon University, Pittsburgh, PA, 15213*

[4]*Department of Biomedical Engineering, University of North Carolina at Chapel Hill, Chapel Hill, NC 27599*

[5]*Department of Radiology, University of North Carolina at Chapel Hill, Chapel Hill, NC 27599*

**ABSTRACT:** Modern polymer science is plagued by the curse of multidimensionality; the large chemical space imposed by including combinations of monomers into a statistical copolymer overwhelms polymer synthesis and characterization technology and limits the ability to systematically study structure–property relationships. To tackle this challenge in the context of $^{19}$F MRI agents, we pursued a computer-guided materials discovery approach that combines synergistic innovations in automated flow synthesis and machine learning (ML) method development. A software controlled, continuous polymer synthesis platform was developed to enable iterative experimental–computational cycles that resulted in the synthesis of 397 unique copolymer compositions within a six-variable compositional space. The non-intuitive design criteria identified by ML, which was accomplished by exploring less than 0.9% of overall compositional space, upended conventional wisdom in the design of $^{19}$F MRI agents and lead to the identification of >10 copolymer compositions that outperformed state-of-the-art materials.

## INTRODUCTION:

Next-generation challenges in soft materials will require the discovery of polymers that perform multiple functions simultaneously. Copolymerization, where two or more building blocks are included in a single material, is an effective strategy to achieve differentiated properties.[1] The inclusion of multiple unique building blocks into a copolymer, however, often has interdependent effects on reactivity, structure, and properties, making *a priori* prediction of material function for complex copolymers challenging.[2] Additionally, traditional synthetic technology in polymer science is iterative, labor-intensive, capricious, and low throughput, making rapid experimentation, purification, and analysis impractical.[3] Polymer science remains plagued, therefore, by the "curse of multidimensionality", where even simple combinations of monomeric building blocks lead to a high-dimensional chemical space that is too vast to explore without implementing limiting assumptions.

Computer-guided materials discovery has been shown to be an effective approach to detect meaningful patterns in datasets of high dimensionality; thus, allowing the prediction of structure–function relationships while only requiring a small percentage of the chemical space to be experimentally explored.[4] One such approach is the use of computer simulations to define molecular structure–property relationships and target specific polymer compositions.[5] However, human intuition defines the inputs of these computational models, which restricts the diversity of the dataset due to inherent biases or limitations in knowledge. Furthermore, computational and experimental cycles are often physically and temporally separated, which slows the speed of chemical structure optimization to achieve desired performance.

The use of Artificial Intelligence (AI) for computer-guided materials discovery is an alternative approach that holds the promise to dramatically accelerate the optimization of polymer

structure–property relationships, with the opportunity to close the loop between computational and experimental components of the materials discovery pipeline.[6,7] Recent advances in both automated synthetic platforms and machine learning (ML) methods development have enabled experimental systems that provide high quality training data to improve ML models and, at times, are driven by ML recommendations in the areas of small molecule synthesis[8–16] and nanomaterial synthesis[17–22]. In a recent example, the Doyle group demonstrated a Bayesian optimization platform that allows chemists to iterate between experimentation and ML within their standard synthetic workflows, thus providing open-source tools to increase the efficiency of chemical synthesis.[23]

Despite impressive advances using ML for small molecule and nanomaterial synthesis, the integration of synthesis, characterization and ML in polymer science has lagged behind.[24–28] A critical challenge is sourcing high quality experimental data to train predictive ML models, which often requires a combination of high-throughput synthesis, purification, and characterization methods that remain underdeveloped in polymer chemistry.[29,30] As an added challenge, the field of polymer science lacks a standardized data schema for reporting polymer structure and properties that contextualize the underlying measurement and its output.[31–33] Applications of ML in polymer science, therefore, have mostly been isolated to a small subset of commonly reported properties[34–36] or relied on legacy data collected within a single research group.[37–39] In a seminal report, Pruksawan *et al.* demonstrated the utility of synthesis and property evaluation of 42 epoxy adhesive samples and employed ML to generate a predictive model that accurately described the performance of 256 possible formulations.[40] In complementary work, Reineke and coworkers made a multiparametric library of 43 copolymers to serve as gene-delivery vectors,[30] and separately Appel and coworkers synthesized a combinatorial library of 172 acrylamide hydrogels

as anti-biofouling coatings.[29] Both groups used random forest classifiers to identify non-intuitive descriptors that led to high performance. In these examples, however, the reliance on labor-intensive batch synthesis or formulation, the need to probe a large percentage (>15%) of the compositional space to optimize an accurate model, and the lack of iterative experimental–computational cycles limit the translation of this approach to more complex problems in high-dimensional copolymer compositional space.

We identified the discovery of high contrast $^{19}$F MRI agents as a challenge in need of a ML-driven discovery approach. $^{19}$F MRI is a high contrast biomedical imaging modality with the potential to track cellular transport and quantitate oxygenation with spatiotemporal resolution.[41–45] Synthetic polymers represent attractive $^{19}$F MRI agents due to their potential for multivalent displays of $^{19}$F atoms and their synthetic modularity. Despite decades of effort reporting hundreds of copolymer $^{19}$F MRI agents, challenges persist to develop $^{19}$F MRI agents that are both water soluble and contain enough fluorine nuclei to be visualized on clinical 3 Tesla (T) MRI scanners.[46]

Herein, we developed automated tools to interface copolymer synthesis and characterization with ML, which enabled iterative feedback through numerous experimental–computational cycles. The nuanced structure–property trends uncovered through this ML-guided materials discovery approach upended the dogma that $^{19}$F solution concentration is directly related to signal intensity in $^{19}$F MRI measurement and proposed non-intuitive design elements that are critical to consider for next-generation $^{19}$F MRI agents. This combination of continuous flow chemistry and ML represents a powerful approach to tackle high-dimensional challenges in polymer science where the large number of interdependent variables makes structure–property relationships difficult to predict or model.

## Results and Discussion

### Development of ML Approach

Given the limited initial $^{19}$F MRI dataset available to build a predictive ML model, we envisioned developing a platform that iterates between computational (*i.e.* software) and experimental (*i.e.* hardware) components to efficiently screen for high performing $^{19}$F MRI agents (Figure 1). The choice of a computational approach proved to be challenging due to the conflicting performance criteria inherent to copolymers used as $^{19}$F MRI agents. The necessity for an imaging agent to possess a high density of hydrophobic fluorinated comonomers while also remaining water soluble demands the optimization of multiple objectives simultaneously along a tradeoff curve, otherwise known as a Pareto front.[47]

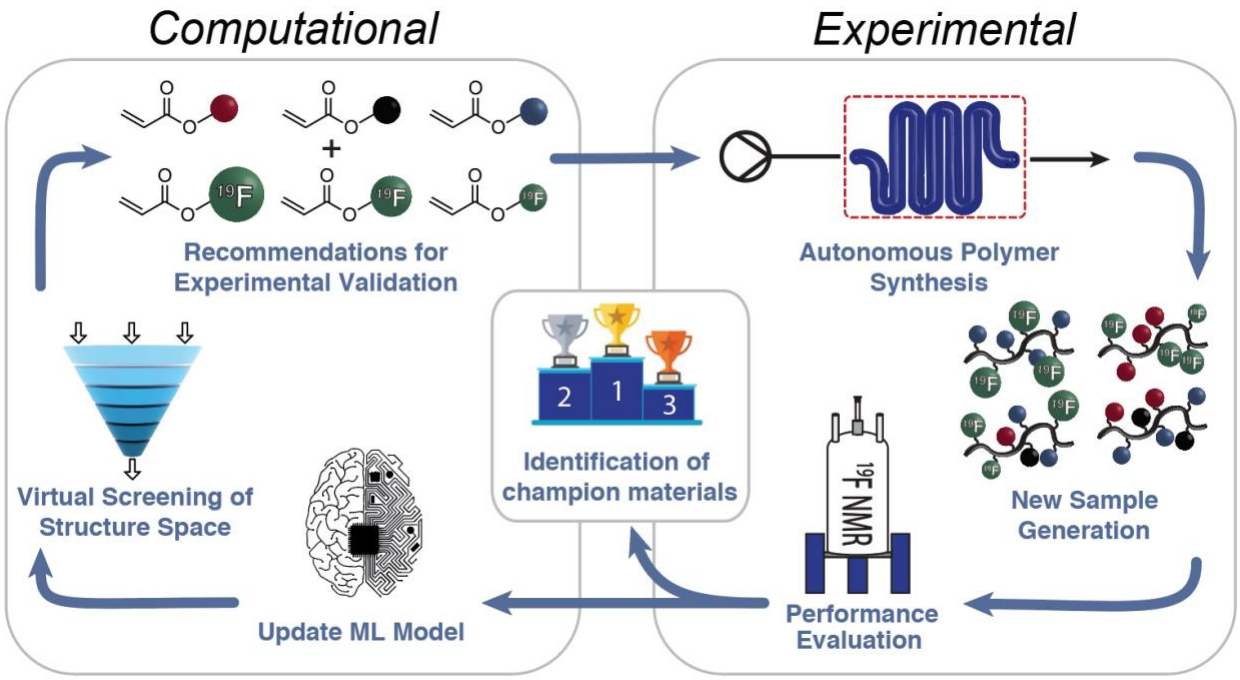


**Figure 1.** The active-learning-guided discovery of copolymer $^{19}$F MRI agents relies on rapid feedback between computational and experimental nodes.

The capability to iterate between experiments and ML allowed us to leverage active learning (AL) for multi-objective optimization.[48] AL is a semi-supervised form of ML where the algorithm efficiently explores chemical space by selecting maximally informative materials to evaluate through experimentation (*i.e.* exploration) or more narrowly identifies high performing compositions (*i.e.* exploitation).[48] Our attempt to implement AL, however, exposed a weakness in the ML pipeline; almost all ML models are designed and tuned by hand, and there is no single ML model that works for all applications. Typically, a manuscript will report only the successful application of a particular method, but tuning these methods to a particular application inherently introduces model and sample selection biases. This leads to researchers selecting suboptimal models or investing a significant amount of time into model tuning for a particular application.

We hypothesized that an automated ML (AutoML) approach would streamline model development and allow a non-expert to search for a high-quality ML model independently.[49] A variety of approaches to AutoML have been developed recently that involve selecting an optimal ML algorithm, preprocessing input features, and selecting hyperparameters, including an extension of the scikit-learn library with meta-learning and ensemble construction[50] and the use of genetic algorithms in the TPOT library.[51] Our AutoML composite approach screens several validated ML learning methods including Gaussian Process, Random Forest, Linear and Logistic Regression, as implemented in scikit-learn,[52] XGBoost,[53] and NGBoost.[54] Here we consider only the supervised learning setting. The models used are limited to fixed-length vectorial representations of the polymer composition and analytical characterization data (See SI for a technical description).

The overall design of AutoML was expressed as a black-box optimization problem to optimize two objectives simultaneously. In such an AutoML workflow, the user provides data,

then the AutoML library autonomously samples aforementioned methods, selects the optimal ML model parameters for the dataset, and makes decisions about subsequent exploratory or exploitative experiments in real time. Overall, the automated ML cycle consists of four steps that can operate in a closed-loop fashion with the appropriate synthetic hardware: *i)* train a proxy AutoML model to optimize for a given set of objectives on an initial dataset; *ii)* use the model selected by AutoML to virtually screen the copolymer compositional space; *iii)* select a subset of copolymer compositions that would increase accuracy of the model; and *iv)* perform synthesis and experimental measurement of selected polymers and use this data to update the ML model(s).

**Design and Implementation of Automated Continuous Flow Copolymer Synthesis**

We identified continuous-flow chemistry as an ideal experimental platform for the iterative synthesis of novel copolymer materials due to its ease of automation, reproducible control of reaction conditions, potential for closed looped optimization between synthesis and analysis, and simple translation to manufacturing scales.[55–62] A majority of previously reported high throughput copolymer synthesis systems polymerize one sample at a time and, thus, require extremely short reaction times to achieve a high sample throughput. For example, Hedrick and coworkers developed a flow reactor capable of synthesizing 100 unique block copolymers in 8 minutes, but the technology relied on ring-opening polymerizations with reaction times of <1 second.[63] Unfortunately, the controlled radical polymerization techniques traditionally employed to make copolymer $^{19}$F MRI agents suffer from reaction kinetics that are orders of magnitude slower than this example,[45,64] which required the design of a novel high-throughput flow reactor.

To combat the challenge of slow copolymerization kinetics, we designed a more general flow platform capable of polymerizing multiple samples simultaneously. We identified droplet

flow as an enabling approach to achieving high sample throughput regardless of polymerization kinetics. Droplet-based flow systems manipulate discrete volumes of reaction mixtures that are separated by an immiscible inert fluid.[56,65–67] As our lab demonstrated previously, polymerization in droplets reduces the residence time distribution and improves control of polymer composition, molar mass ($M_n$), and dispersity.[61] For this application, nitrogen gas was used as the immiscible fluid between large reaction droplets, or slugs. A custom liquid handler was fabricated that allowed precise formulations to be loaded into a sample loop before being injected into the heated reactor. Through experimentation we discovered that a wash slug of DMF was required between sequential reaction slugs to prevent cross-contamination. A simplified schematic of the flow reactor is shown in Figure 2 and a more detailed version is described in the supplementary information (Figure S5).

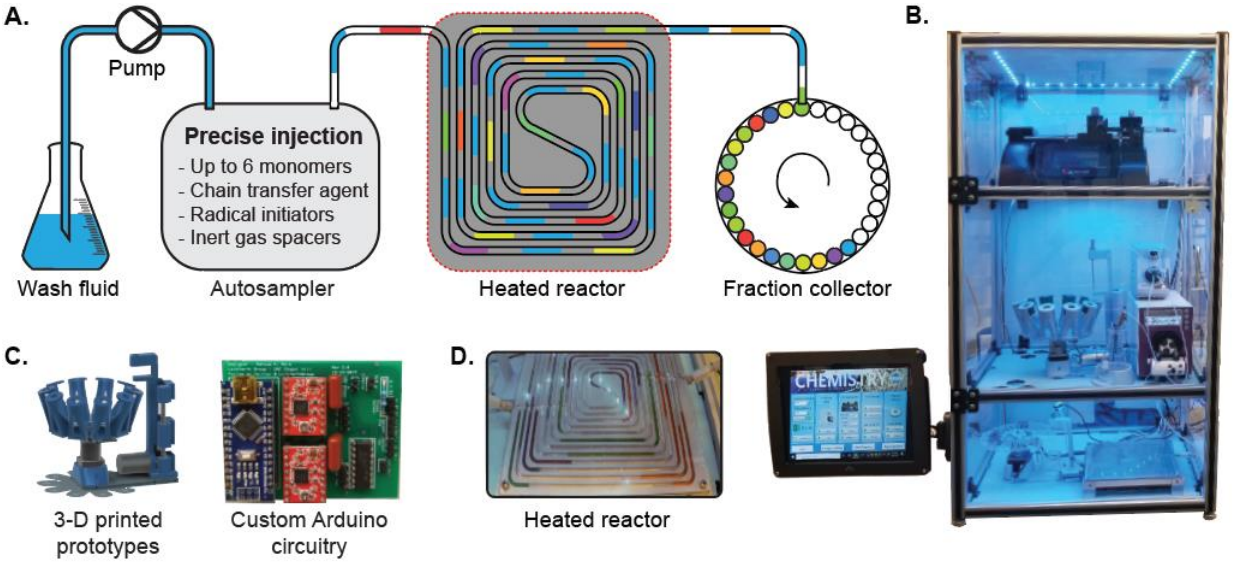


**Figure 2.** Automated continuous-flow reactor development. (A) Simplified reactor schematic. (B) Droplet-flow reactor. (C) Rapid prototyping enabled by 3-D printed hardware and a modular electronics platform. (D) Demonstration of droplet technology using colored dyes, videos found in supplementary information.

To create a modular platform that could access a broad compositional space in a user-friendly fashion, the reagent selection, comonomer formulation, slug injection sequence, and sample collection were fully automated using custom hardware and software (See supplementary videos for visualization). An Arduino microcontroller was chosen as the electronics platform to control the flow system, and integration of all individual components with LabVIEW software allowed full automation of complex reaction sequences. The use of readily accessible electronics and 3-D printed parts allowed for the rapid design and prototyping of hardware components optimized for high throughput copolymer synthesis. The custom liquid handler enabled the efficient and precise formulation of reaction slugs containing radical initiators, up to six different comonomers, and a compatible RAFT chain transfer agent. To achieve droplet-flow, each 300 µL reaction slug is confined on both sides by two nitrogen slugs and loaded into the sample loop of a two-position six-port switching valve. At a pre-determined point during the automated reaction sequence these slugs are injected into the flow stream. The heated reactor consisted of tubing embedded in a machined aluminum block, with a heating element and thermocouple to provide accurate temperature regulation. Upon exiting the reactor, samples are collected in a 30-slot sample collection carousal. Rotation of the carousal is triggered by a refractive index (RI) detector immediately upstream, which tracks the number of eluted slugs by monitoring the change in RI between reaction slugs and nitrogen slugs.

The entire droplet flow system occupies a small footprint (43 cm by 46 cm by 96 cm) and is fully touch screen enabled to allow use by non-experts. LabVIEW software controlling the flow reactor is capable of extracting relevant reaction parameters from comma separated value (CSV) files generated by the user or the AL algorithm. The combination of these efforts afforded an easy-to-use system capable of synthesizing a new copolymer composition every two minutes, allowing

the synthesis of 30 unique copolymers in two hours using only 12 mL of reaction solution. The typical workflow for synthesis, purification, and analysis was optimized to evaluate batches of 30 unique $^{19}$F MRI contrast agents. This workflow consisted of *i)* preparation of monomer stock solutions, *ii)* automated synthesis of copolymers in flow, *iii)* transfer of samples to gravity fed SEC columns, *iv)* drying of polymer containing fractions, and *v)* $^{19}$F NMR analysis and data work-up. Not including drying times, this method allowed the evaluation of 30 samples in a single 8-hour workday. To evaluate the reproducibility of this workflow, twenty representative compositions were run in triplicate and the tabulated results can be found in table S4. The accumulative errors across all steps of the workflow resulted in a modest average standard deviation of four SNR units across the studied copolymer samples. Additionally, the automated and modular flow platform described herein will enable simple expansion to accommodate new chemistries and reaction sequences.

**Synthesis and Characterization of Copolymer $^{19}$F MRI agents**

The inherent tension between having a high density of hydrophobic fluorine atoms while maintaining water solubility for $^{19}$F MRI agents has been solved in previous literature through the statistical copolymerization of partially fluorinated monomers such as trifluoroethyl acrylate (TFEA) with hydrophilic monomers such as poly(ethylene-glycol) acrylate (PEGA) to afford $^{19}$F MRI agents with moderate sensitivity.[64,68–77] These copolymers provided adequate materials for pre-clinical studies on high-resolution spectrometers, but did not demonstrate the required sensitivity to be used on 3 T clinical-strength MRI instruments at realistic concentrations. Previous work has identified that a number of different hydrophilic and partially fluorinated comonomers can improve $^{19}$F MRI sensitivity in isolated examples, but an understanding of how polymer

composition relates to material performance is lacking.[64,69,73–77] When attempting to data-mine literature examples of $^{19}$F MRI agents to apply ML methods, we encountered challenges standardizing the signal-to-noise ratio for $^{19}$F MRI agents across studies due to differences in magnetic field strength, pulse sequence, reagent concentration, and reporting procedure.

In order to significantly advance the state-of-the-art, we hypothesized that a systematic evaluation of the most promising fluorinated and solubilizing comonomers would provide a more comprehensive understanding of the structure–property relationships that dictate the performance of $^{19}$F MRI agents (Figure 3A). The partially fluorinated acrylic comonomers chosen include TFEA as well as the more densely fluorinated hexafluorooxy-ethylacrylate and nonafluorooxy-ethylacrylate (HexaFOEA and NonaFOEA, respectively). The water solubilizing acrylic comonomers include PEGA as well as 2-(methylsulfiyl)ethyl acrylate and hydroxyethyl acrylate (MSEA and HEA, respectively).

Copolymerization using thermally initiated reversible addition-fragmentation chain-transfer (RAFT) was selected due to its tolerance of diverse functionality as well as its ability to provide control over the copolymer molar mass ($M_n$) and dispersity ($Đ$). A similar degree of polymerization (DP) was targeted for each copolymer $^{19}$F MRI agent to decrease the potential for chain-length effects to influence material performance. A common challenge for high-throughput radical polymerization is the need to rigorously remove oxygen from each sample and, thus, limit batch to batch variability.[78–98,99–105] We took inspiration from the "polymerizing through" approach[106–110] to oxygen-tolerant RAFT polymerization where a large flux of radicals is introduced at the start of the reaction to consume dissolved oxygen, and a smaller and consistent radical flux subsequently provides controlled polymerization. A high radical flux was achieved through the addition of a low concentration of V-70, an azo radical initiator with a short half-life at the reaction

temperatures, in addition to the more typical radical initiator AIBN (See SI for detailed copolymerization methodology).

Following copolymer synthesis, we recognized that copolymer purification presented a potential bottleneck to the exploration of large compositional space. Precipitation was not broadly applicable because copolymers of different compositions possessed different solubilities, and dialysis was impractical in a high-throughput fashion. A purification procedure using aqueous SEC gravity desalting columns proved to be ideal.[111] The workflow included taking polymer samples directly from the reaction and eluting them with a known amount of deionized water through the SEC column. This approach allowed for multiple polymers to be purified in parallel and excluded water insoluble copolymers that precipitated within the resin.

The figure-of-merit chosen to evaluate the performance of multicomponent polymers as $^{19}F$ MRI agents was the signal-to-noise (SNR) ratio taken from 1D $^{19}F$ experiments on a 400 MHz NMR. These SNR values for $^{19}F$ NMR correlate with $^{19}F$ MRI sensitivity, with small variations that result from differences in pulse sequences and probe design.[112] Copolymer samples were diluted with phosphate buffered saline (PBS) solution/$D_2O$ (90:10, v/v) at a concentration of 20 mg/mL. Each copolymer composition exhibited unique $^{19}F$ resonances resulting from a combination of factors that include copolymer composition and copolymer solution conformation (Figure 3B). The unique chemical environment resulting from the copolymer solution structure influences $^{19}F$ chemical shift values ($\delta$) and spin-lattice relaxation times ($T_1$), with shorter $^{19}F$ $T_1$ increasing the signal-intensity observed during $T_1$-weighted MRI sequences. Furthermore, polymers with high fluorinated comonomer content demonstrate significant peak broadening as a result of short spin-spin relaxation ($T_2$). The interdependent properties that contribute to the SNR

value of multicomponent copolymers, therefore, are difficult to predict *a priori* and require experimental validation.

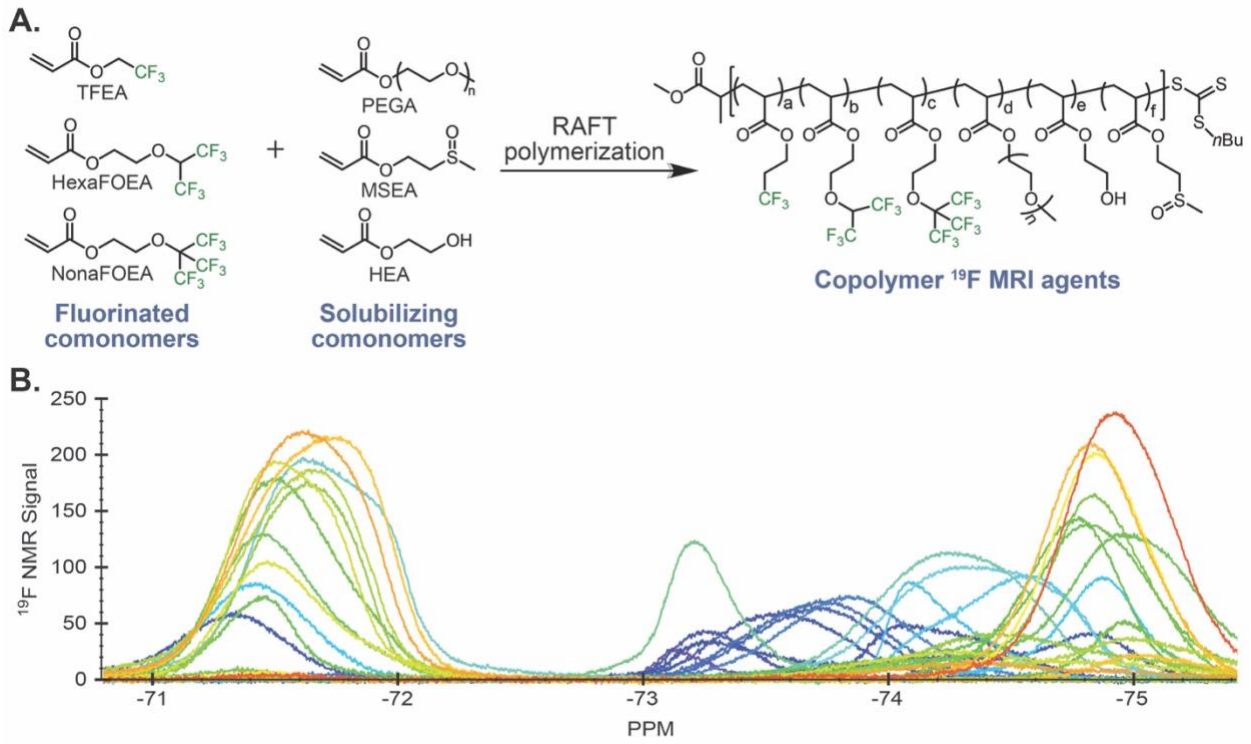


**Figure 3.** Synthesis of multicomponent copolymers as $^{19}$F MRI agents. (A) Six comonomers were chosen to synthesize statistical copolymers while balancing $^{19}$F content and water solubility; (B) The $^{19}$F NMR spectra of 30 representative copolymers demonstrating the diversity of resonances arising from different copolymer compositions.

## Implementation of ML-guided Discovery of Champion $^{19}$F MRI Agents

While the six comonomers in Figure 2A established the compositional space for exploration, we sought to establish a number of boundary conditions to define the specific copolymer structures for synthesis and evaluation. First, the individual comonomer compositions would change by increments of 5%. Smaller shifts in composition were at the limit of our liquid

handling technology. Second, the comonomers and CTA chosen produced only linear polymers, thus removing the potential for polymer topology to influence performance. Third, all polymerizations were assumed to be statistical, with the initial comonomer stoichiometry being the assumed stoichiometry incorporated into the polymer. Given these boundary conditions, the experimental exploration of six unique monomers revealed 47,854 possible copolymer compositions to explore. At every batch the AutoML algorithm selected optimal features from a range of representations, which includes a vector of monomer fractions of length 6 for each composition (one-hot encoding; the sum of all 6 fractions of polymer composition equals 1 for each composition), fraction of fluorine, and various constitutional descriptors from RDKit (See SI for a technical description).

Typical ML approaches require a large portion of the overall chemical space to be explored (>5%) before converging onto an accurate model, which in our case would have required the synthesis of an impractical number (>2200) of individual copolymers. We hypothesized, since polymer composition is a continuous variable whose boundary conditions can be adjusted, that a *hierarchical sampling of compositional space* would be a more efficient approach. Therefore, initial screening focused on a coarse compositional space where individual comonomer compositions could only change in 10% intervals, shrinking the explorable compositional space from 47,854 to 2,486 possible copolymer combinations. We hypothesized that this would allow model development with a smaller library of initial data points, and, as model performance improved, a switch to the larger compositional space of 47,854 potential copolymers with a 5% change in comonomer composition (fine compositional space) would be feasible. Furthermore, we required an approach that not only predicted SNR for $^{19}$F MRI, but also overlaid that model with

one that predicted the water solubility. Therefore, both properties are used for multi-objective optimization.

Our AL experiments were initialized from data containing 157 copolymers compositions, which represents 6.3% of the course compositional space. This initial dataset was gathered from materials made previously in our lab[45], which targeted high performing imaging agents, as well as samples made during instrument optimization (Figure 4A). To simultaneously optimize for water-solubility and SNR, we used two separate ML models; the first was a classification model that predicted whether or not a sample would be water soluble, and the second was a regression model that predicted $^{19}$F NMR SNR values. To balance exploration and exploitation we used spherical exclusion clustering[113] to reduce the number of candidate compositions to an experimental batch size of 30 while ensuring reasonable composition diversity. After running the system for two AL cycles, the mean absolute error (MAE) decreased to below eight SNR units and stabilized. Given the increasingly accurate model performance in the coarse compositional space, we sought to exploit the model to select high performing materials in the larger compositional space of 47,854 potential copolymers (Figure 4, batch 3). This initial effort, which included data from only 0.45% of the fine compositional space, led to an experimental batch of 30 copolymers that were all insoluble in water.

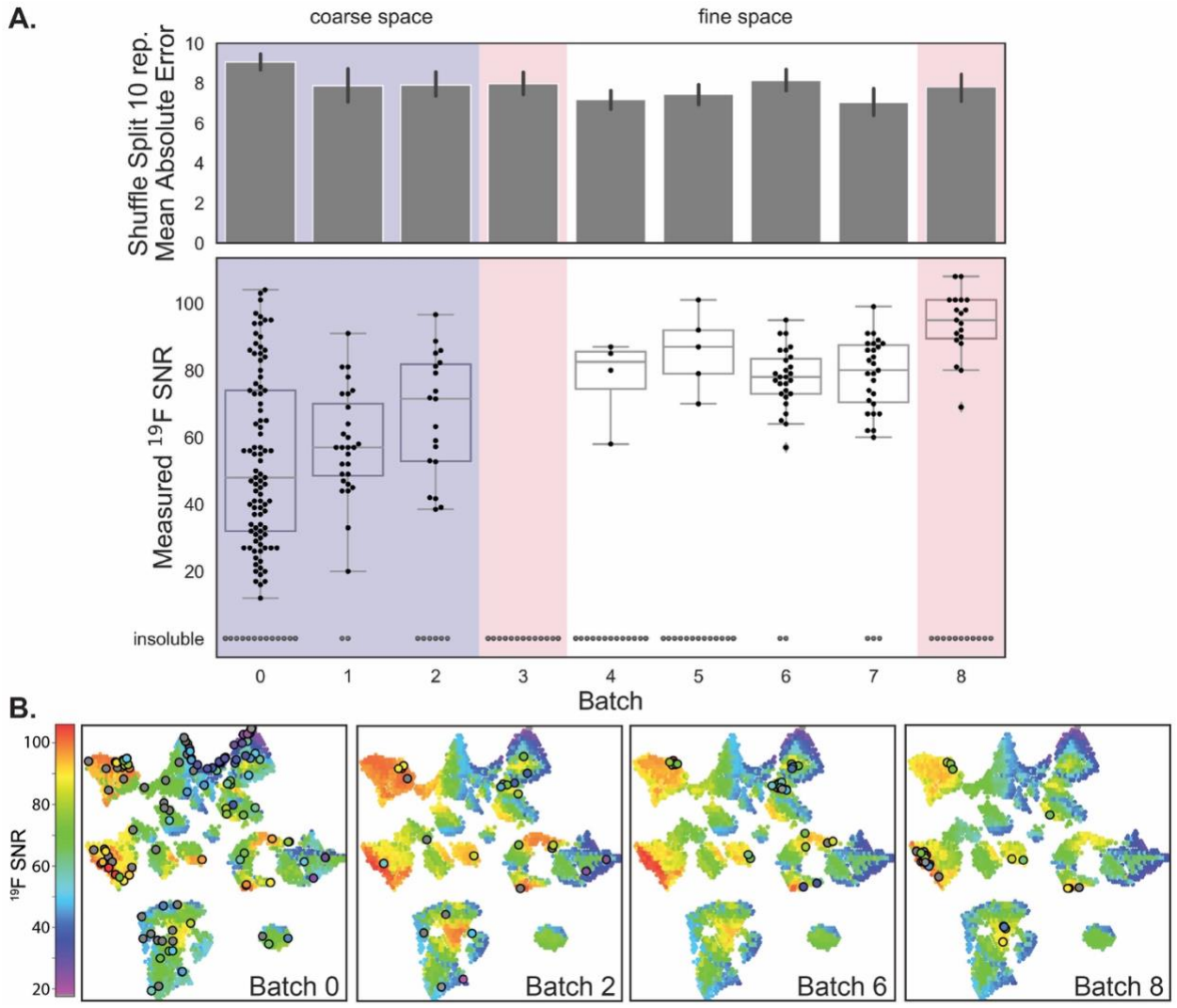


**Figure 4. (A)** Data acquisition and ML model performance throughout the AL steps. The top panel shows the MAE error for $^{19}$F SNR ML models; confidence intervals are obtained through 10 shuffle splits. The bottom panel show actual data points and corresponding box plots for the data distribution. The insoluble materials are depicted as gray points at the bottom, and the total number of molecules per batch is equal to 30 in batches 1-8. The experiments using the coarse compositional space (10% step) are highlighted in purple and fine compositional space (5% step) are white. The batches run targeting exploitation are colored in pink. (B) Uniform manifold

approximation and projection (UMAP) of representative batches. Colored circles represent water soluble structures experimentally validated and grey circles represent insoluble samples.

As evidenced by the poor performance of batch 3, moving from a course (10% interval) to a fine (5% interval) compositional space required more experimental data points. For batch 4 we synthesized 30 copolymers to target exploration of the fine compositional space. The SNR predictions remained quite accurate, but the multi-objective optimization that included solubility required a significant number of experimental results to converge. As shown in Figure 4A, batch 3 and batch 4 resulted in the synthesis of many insoluble samples as the algorithm worked to define solubility parameters. Three additional rounds of exploration (batches 5–7) improved predictive power and resulted in an AL model that could accurately predict the SNR values of soluble copolymers with a mean absolute error of < 7 SNR units. Given the experimental error of the automated synthesis system is 4 SNR units, the model reached a high value of accuracy. A selection of the samples identified by the algorithm in each batch and experimentally produced by the flow system is shown in Figure 4B (full representation in Figure S2).

To study the influence of molecular weight on copolymer $^{19}$F MRI performance, a large subset of the data was analyzed by size exclusion chromatography (SEC) and polymer $M_n$ and $Đ$ were calculated. The $M_n$ values were used as an input for the ML model (Figure S6), but no statistically significant effect on predicting material performance was identified. Given that all polymerizations targeted the same DP, the modest differences in $M_n$ did not influence polymer $^{19}$F MRI agent sensitivity.

Providing the increasingly accurate model predictions, we initiated an exploitation AL cycle by having the model greedily select $^{19}$F MRI agents with potentially high performance (batch

8). The batch of 30 samples included 15 copolymers with an SNR over 80 and two that exceeded the values of the highest performing copolymers reported in our previous study. The batch also included 11 samples that were insoluble, which represented a significant improvement over the attempt at exploitation prior to model development in the larger compositional space. Overall, this hierarchical AL model development workflow produced a robust model to predict the structure–performance relationships of 47,854 potential copolymer $^{19}$F MRI agents while experimentally exploring < 0.9% of compositional space (397 copolymers).

**Analysis of Compositional Space and Structure–Property–Performance relationships**

The central dogma in this field is that copolymers with higher $^{19}$F content have higher SNR in $^{19}$F MRI experiments.[45,64,74,76,77] Considering the three partially fluorinated monomers chosen for this study (Figure 2A), and our previous observations[45], we hypothesized that copolymers made with NonaFOEA would have the highest sensitivity given NonaFOEA has the highest weight percent (wt%) $^{19}$F. The parallel coordinate diagram in Figure 5A collects data for copolymer composition, wt% $^{19}$F, and SNR for each copolymer produced in this study. Initial evaluation of this data demonstrated an unexpected but clear discontinuity between wt% $^{19}$F and SNR. To describe these effects in more detail, comparing a few representative copolymers is instructive. Copolymer **1**, which was identified by the ML model during the AL exploitation step (batch 8), represents the highest performing copolymer (SNR of 111). The sample, along with >80% of the samples that achieved an SNR > 100, had HexaFOEA as the fluorine-containing comonomer. Copolymer **1** contained only 21.6 wt% fluorine yet outperformed the dozens of copolymer samples that contained higher fluorine density. Copolymer **1** also contained more than one solubilizing

comonomer, which is a trend we observed for most high performing copolymers and has not been demonstrated in previous studies.

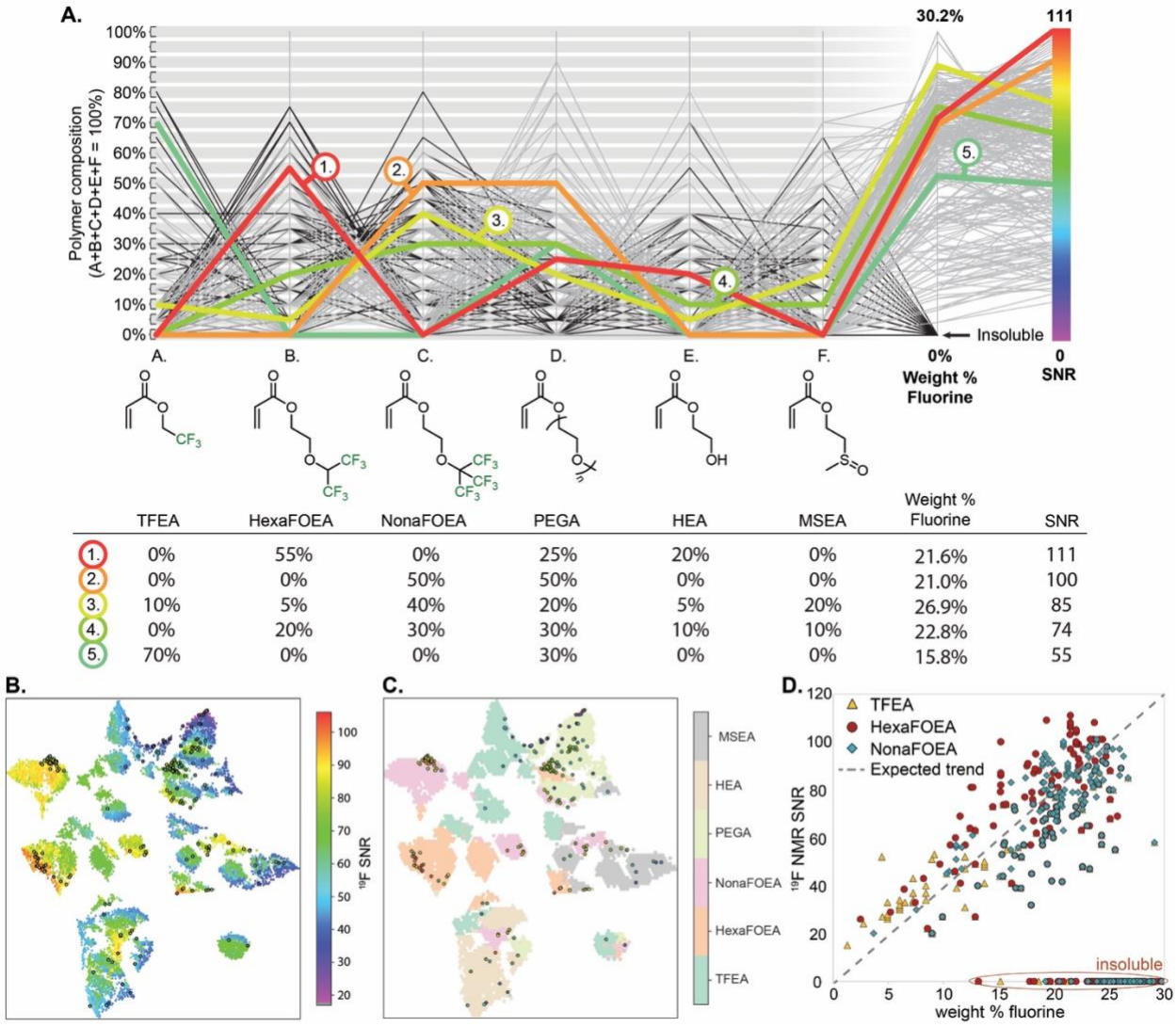


| | TFEA | HexaFOEA | NonaFOEA | PEGA | HEA | MSEA | Weight % Fluorine | SNR |
|---|---|---|---|---|---|---|---|---|
| 1. | 0% | 55% | 0% | 25% | 20% | 0% | 21.6% | 111 |
| 2. | 0% | 0% | 50% | 50% | 0% | 0% | 21.0% | 100 |
| 3. | 10% | 5% | 40% | 20% | 5% | 20% | 26.9% | 85 |
| 4. | 0% | 20% | 30% | 30% | 10% | 10% | 22.8% | 74 |
| 5. | 70% | 0% | 0% | 30% | 0% | 0% | 15.8% | 55 |

**Figure 5.** Visualization of experimental $^{19}F$ compositional space; (A) Parallel coordinate diagram of the 397 samples that describes copolymer composition and performance, with six representative compositions colored and shown in table format. (B) UMAP projection of the copolymer compositional space with $^{19}F$ SNR ML prediction color coded. Circled samples represent water soluble structures experimentally validated. (C) UMAP projection of the copolymer compositional space with the major comonomer component color coded. Circled samples represent water soluble

structures experimentally validated. (D) Plot demonstrating the relationship between the wt% $^{19}F$ in soluble copolymers and the $^{19}F$ NMR SNR.

Comparing **1** to other copolymers provides comparative structure–property information. Copolymer **2** was synthesized in batch 0 and contains approximately the same wt% fluorine at **1**, but the use of NonaFOEA instead of HexaFOEA and lack of solubilizing monomers beyond PEGA results in a lower SNR of 100. Copolymers **3** and **4** both have higher wt% fluorine than **1**, but the higher fluorine density is the result of a combination of partially fluorinated monomers in the copolymers, which limits the SNR of any one $^{19}F$ resonance. Lastly, copolymer **5** demonstrates the limitations of TFEA to achieve high SNR despite its high mol% incorporation.

Figure 5B shows a two-dimensional UMAP of the complete compositional space of all possible copolymers.[114] UMAP estimates a topology of the high-dimensional data and uses this information to construct a low-dimensional representation that preserves relationships present in the data. The computationally derived SNR values are represented by the color gradient in the image, while the soluble copolymers samples that were produced experimentally are represented as circular icons (UMAP including soluble and insoluble samples in Figure S3). Most striking in this image are the many disconnected "islands" within the chemical space where high SNR copolymers are located. Considering this plot in tandem with the representation of chemical composition (Figure 5C and Figure S4) demonstrates that high-performing copolymers predominately contain HexaFOEA and NonaFOEA but identifying a pattern for the non-fluorinated comonomers that lead to high SNR is non-intuitive.

A visualization of the unexpected structure–property trends can be seen in Figure 5D. The occurrence of a large population of copolymers containing HexaFOEA above the expected linear

trend between wt% $^{19}F$ and SNR demonstrates its privileged selection as a fluorinated comonomer. Additionally, the complexity of structure–solubility relationships is evident by the many insoluble copolymer compositions that have the same wt% $^{19}F$ as high performing materials. Regression analysis (Figure S11) of the soluble copolymers provides quantitative evidence of the privileged nature of HexaFOEA-containing copolymers. The $R^2$ values are 0.67 and 0.39 for TFEA-containing copolymers and HexaFOEA-containing copolymers, respectively, revealing how the linear relationships between wt% $^{19}F$ and SNR is less evident for HexaFOEA. These results underscore the importance of high-throughput synthesis coupled to ML-guided materials design, especially for identifying materials that display non-intuitive structure–property relationships.

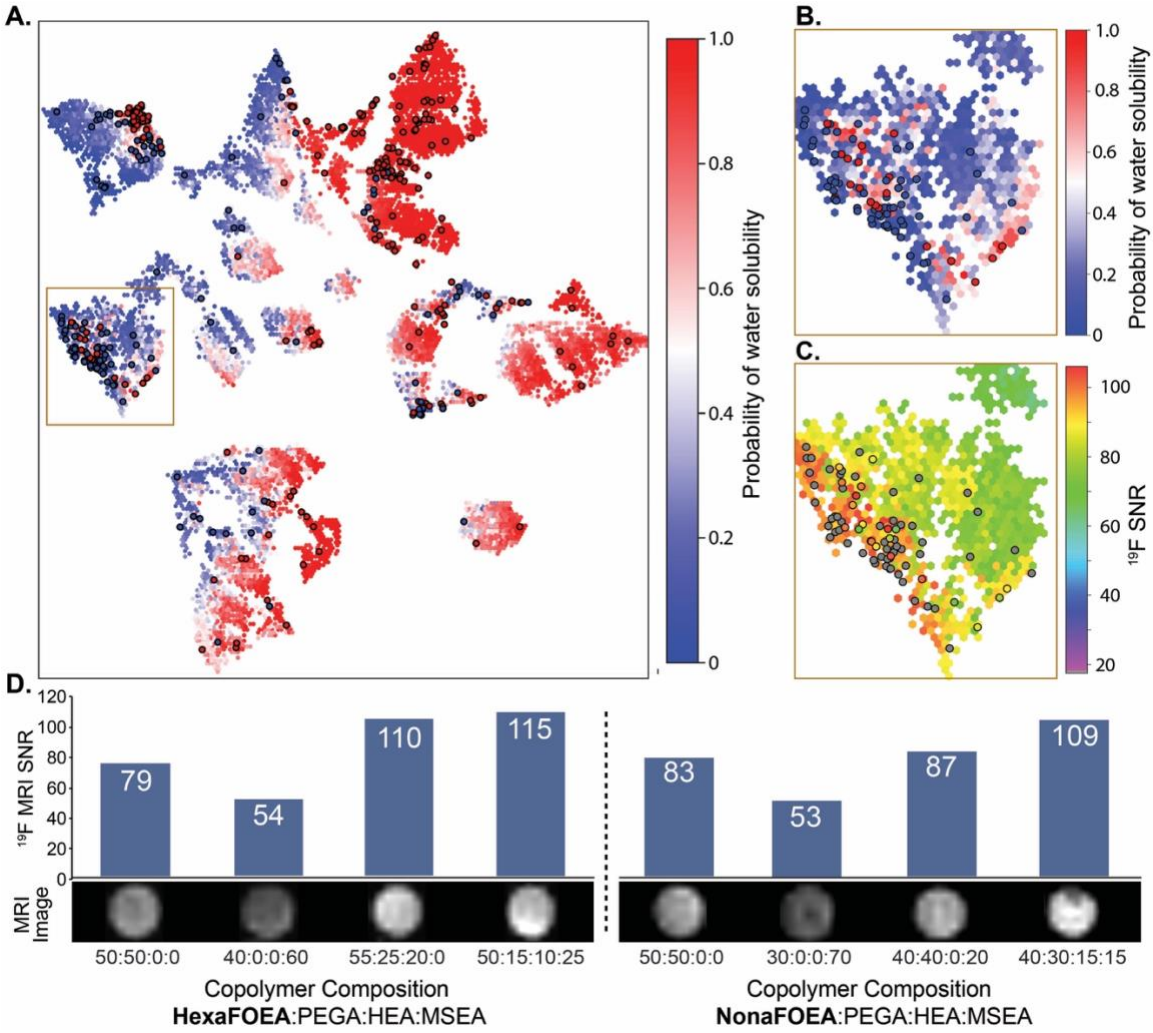


**Figure 6.** (A) UMAP representation of copolymer compositional space with ML algorithm predictions for water solubility color coded. Experimentally validated samples are color coded. (B and C) Zoomed-in portion of the copolymer compositional space where the highest performing copolymers resided. Comparison of the water solubility (B) and SNR (C) models within this area of interest. (C) $^{19}$F MRI analysis of eight representative copolymer samples, including SNR values and phantom MR images.

Contextualizing the ML model outputs by comparing both the SNR and solubility predictions reveals the complexity of identifying high-performing $^{19}$F MRI agents (Figure 6A). The "islands" where high SNR is predicted overlay quite closely with areas in which few copolymers are predicted to be soluble, which is expected due to the intrinsic relationships between

fluorine density and hydrophobicity. A more detailed visualization in Figure 6B–C shows a zoom-in on the western region of the chemical space, with both the SNR and water solubility prediction shown. The solubility prediction clearly shows the complex geography of the chemical space where high SNR and water solubility coincide. Without the aid of ML, discovering the ideal combination of comonomers to yield a soluble copolymer is this region is unlikely. We hypothesize that the non-intuitive relationship between polymer composition and solubility is due to the subtle influence that sequence and comonomer identity can have on the solution conformation of a flexible polymer chain, and thus the functionality present on the exterior of the globule that must interact with water to maintain solubility.

Eight representative copolymers with a range of SNR values and compositions were selected for analysis using application-specific techniques. These included evaluation of $^{19}$F NMR $T_1$ and $T_2$ relaxation times as well as MRI imaging using a $T_1$-weighted fast low angle shot (FLASH) pulse sequence[115,116] (Figure 6D, Tables S2 and S3). These MRI studies confirmed a number of observations that the ML algorithm identified. First, copolymers that contained three or more comonomers generally outperformed two-component copolymers, which we hypothesize is a result of the difficulty for fluorinated moieties to segregate into dense phases within a compositionally complex polymer globule. Second, although previous work[117] set a detection limit of 126 mM $^{19}$F for visualization on a 3 T clinical MRI scanner, we demonstrate that concentration of $^{19}$F alone is not an accurate predictor of $^{19}$F MRI sensitivity. For example, the highest performing HexaFOEA and NonaFOEA multicomponent copolymers, containing a concentration of ~240 mM $^{19}$F and 230 mM $^{19}$F, respectively, both displayed nearly 1.4 times higher $^{19}$F MRI SNR than the highest sensitivity previously reported, which used NonaFOEA at a concentration of 220 mM $^{19}$F. Therefore, the increase in $^{19}$F MRI SNR cannot be solely attributed to an increase in the

concentration of fluorine nuclei, and further illustrates the interdependent nature of the variables responsible for $^{19}$F MRI sensitivity. Lastly, both HexaFOEA and NonaFOEA copolymers reached a limit in achievable $^{19}$F MRI SNR at 240 mM $^{19}$F, which could represent the threshold of fluorine concentration before water-insolubility and detrimental $^{19}$F $T_2$ broadening impact MRI sensitivity.

**Conclusion**

We demonstrated an ML-guided materials discovery approach that combines synergistic innovations in automated flow synthesis and ML method development. Iterative feedback between polymer synthesis, characterization, and ML, combined with a hierarchical exploration of compositional space, enabled the development of an ML algorithm that accurately predicts structure–property relationships while only requiring <0.9 % of the compositional space (397 copolymers) to be experimentally explored. Our approach facilitated the discovery of a number of copolymeric $^{19}$F MRI agents with imaging sensitivities higher than previously reported materials. Additionally, the trends uncovered herein have upended the dogma that $^{19}$F concentration is directly related to signal intensity in $^{19}$F MRI measurement. The non-intuitive material design elements for $^{19}$F MRI agents identified in our study, including the privileged function of HexaFOEA as a fluorinated comonomer, the benefits of using multiple solubilizing comonomers in a single imaging agent, and the observation that wt% fluorine is not directly related to SNR, are critical to consider in the search for next-generation $^{19}$F MRI agents.

Materials discovery typically relies on either luck or human intuition, which both suffer from inherent biases and limitations in knowledge. As this study demonstrates, the continued integration of software-enabled high throughput polymer synthesis and ML represents a powerful approach to accelerate materials discovery, especially in areas of polymer science where the large

number of interdependent variables makes structure–property relationships difficult to predict or model.

**Acknowledgements.**

F. A. L. acknowledges funding from the Beckman Foundation under the Beckman Young Investigator grant. The UNC Department of Chemistry's NMR Core Laboratory provided expertise and instrumentation that enabled this study with support from National Science Foundation (CHE-1828183 and CHE-0922858). O. I. acknowledges support from NSF CHE-1802789 and CHE-2041108. This work was performed, in part, at the Center for Integrated Nanotechnologies, an Office of Science User Facility operated for the U.S. Department of Energy (DOE) Office of Science. The authors acknowledge Extreme Science and Engineering Discovery Environment (XSEDE) award DMR110088, which is supported by NSF grant number ACI-1053575. This research is part of the Frontera computing project at the Texas Advanced Computing Center. Frontera is made possible by the National Science Foundation award OAC-1818253.

**References.**

(1) Moad, G.; Solomon, D. H. Copolymerization. In *The Chemistry of Radical Polymerization*; 2005; pp 333–412.

(2) Li, Y.; Abberton, B. C.; Kröger, M.; Liu, W. K. *Challenges in Multiscale Modeling of Polymer Dynamics*; 2013; Vol. 5.

(3) Oliver, S.; Zhao, L.; Gormley, A. J.; Chapman, R.; Boyer, C. Living in the Fast Lane—High Throughput Controlled/Living Radical Polymerization. *Macromolecules* **2019**, *52* (1), 3–23.

(4) Himanen, L.; Geurts, A.; Foster, A. S.; Rinke, P. Data-Driven Materials Science: Status, Challenges, and Perspectives. *Adv. Sci.* **2019**, *6* (21), 1900808.

(5) Gartner, T. E.; Jayaraman, A. Modeling and Simulations of Polymers: A Roadmap. *Macromolecules* **2019**, *52* (3), 755–786.

(6) Dimitrov, T.; Kreisbeck, C.; Becker, J. S.; Aspuru-Guzik, A.; Saikin, S. K. Autonomous Molecular Design: Then and Now. *ACS Appl. Mater. Interfaces* **2019**, *11* (28), 24825–24836.

(7) Winicov, H.; Schainbaum, J.; Buckley, J.; Longino, G.; Hill, J.; Berkoff, C. E. Chemical Process Optimization by Computer - a Self-Directed Chemical Synthesis System. *Anal. Chim. Acta* **1978**, *103*, 469–476.

(8) Coley, C. W.; Thomas, D. A.; Lummiss, J. A. M.; Jaworski, J. N.; Breen, C. P.; Schultz, V.; Hart, T.; Fishman, J. S.; Rogers, L.; Gao, H.; et al. A Robotic Platform for Flow Synthesis of Organic Compounds Informed by AI Planning. *Science* **2019**, *365* (6453).

(9) Granda, J. M.; Donina, L.; Dragone, V.; Long, D. L.; Cronin, L. Controlling an Organic Synthesis Robot with Machine Learning to Search for New Reactivity. *Nature* **2018**, *559* (7714), 377–381.

(10) Ahneman, D. T.; Estrada, J. G.; Lin, S.; Dreher, S. D.; Doyle, A. G. Predicting Reaction Performance in C–N Cross-Coupling Using Machine Learning. *Science* **2018**, *360* (6385), 186–190.

(11) Trobe, M.; Burke, M. D. The Molecular Industrial Revolution: Automated Synthesis of Small Molecules. *Angew. Chem. Int. Ed.* **2018**, *57* (16), 4192–4214.

(12) de Almeida, A. F.; Moreira, R.; Rodrigues, T. Synthetic Organic Chemistry Driven by Artificial Intelligence. *Nat. Rev. Chem.* **2019**, *3* (10), 589–604.

(13) Strieth-Kalthoff, F.; Sandfort, F.; Segler, M. H. S.; Glorius, F. Machine Learning the Ropes: Principles, Applications and Directions in Synthetic Chemistry. *Chem. Soc. Rev.* **2020**, *49* (17), 6154–6168.

(14) Maryasin, B.; Marquetand, P.; Maulide, N. Machine Learning for Organic Synthesis: Are Robots Replacing Chemists? *Angew. Chemie - Int. Ed.* **2018**, *57* (24), 6978–6980.

(15) Ekins, S.; Puhl, A. C.; Zorn, K. M.; Lane, T. R.; Russo, D. P.; Klein, J. J.; Hickey, A. J.; Clark, A. M. Exploiting Machine Learning for End-to-End Drug Discovery and Development. *Nat. Mater.* **2019**, *18* (5), 435–441.

(16) Gromski, P. S.; Henson, A. B.; Granda, J. M.; Cronin, L. How to Explore Chemical Space Using Algorithms and Automation. *Nat. Rev. Chem.* **2019**, *3* (2), 119–128.

(17) Kusne, A. G.; Yu, H.; Wu, C.; Zhang, H.; Hattrick-Simpers, J.; DeCost, B.; Sarker, S.; Oses, C.; Toher, C.; Curtarolo, S.; et al. On-the-Fly Closed-Loop Materials Discovery via Bayesian Active Learning. *Nat. Commun.* **2020**, *11* (1), 5966.

(18) Epps, R. W.; Volk, A. A.; Reyes, K. G.; Abolhasani, M. Accelerated AI Development for Autonomous Materials Synthesis in Flow. *Chem. Sci.* **2021**, *12* (17), 6025–6036.

(19) Braham, E. J.; Davidson, R. D.; Al-Hashimi, M.; Arróyave, R.; Banerjee, S. Navigating the Design Space of Inorganic Materials Synthesis Using Statistical Methods and Machine Learning. *Dalt. Trans.* **2020**, *49* (33), 11480–11488.

(20) Tabor, D. P.; Roch, L. M.; Saikin, S. K.; Kreisbeck, C.; Sheberla, D.; Montoya, J. H.; Dwaraknath, S.; Aykol, M.; Ortiz, C.; Tribukait, H.; et al. Accelerating the Discovery of Materials for Clean Energy in the Era of Smart Automation. *Nat. Rev. Mater.* **2018**, *3* (5), 5–20.

(21) Volk, A. A.; Epps, R. W.; Abolhasani, M. Accelerated Development of Colloidal

Nanomaterials Enabled by Modular Microfluidic Reactors: Toward Autonomous Robotic Experimentation. *Adv. Mater.* **2021**, *33* (4), 2004495.

(22) Pollice, R.; dos Passos Gomes, G.; Aldeghi, M.; Hickman, R. J.; Krenn, M.; Lavigne, C.; Lindner-D'Addario, M.; Nigam, A.; Ser, C. T.; Yao, Z.; et al. Data-Driven Strategies for Accelerated Materials Design. *Acc. Chem. Res.* **2021**, *54* (4), 849–860.

(23) Shields, B. J.; Stevens, J.; Li, J.; Parasram, M.; Damani, F.; Alvarado, J. I. M.; Janey, J. M.; Adams, R. P.; Doyle, A. G. Bayesian Reaction Optimization as a Tool for Chemical Synthesis. *Nature* **2021**, *590* (7844), 89–96.

(24) Sha, W.; Li, Y.; Tang, S.; Tian, J.; Zhao, Y.; Guo, Y.; Zhang, W.; Zhang, X.; Lu, S.; Cao, Y.; et al. Machine Learning in Polymer Informatics. *InfoMat* **2021**, *3* (4), 353–361.

(25) Kuenneth, C.; Rajan, A.; Tran, H.; Chen, L.; Kim, C.; Ramprasad, R. Polymer Informatics with Multi-Task Learning. *Patterns* **2021**, *2* (4), 100238.

(26) Audus, D. J.; de Pablo, J. J. Polymer Informatics : Opportunities and Challenges. *ACS Macro Lett.* **2017**, 1078–1082.

(27) Jackson, N. E.; Webb, M. A.; de Pablo, J. J. Recent Advances in Machine Learning towards Multiscale Soft Materials Design. *Curr. Opin. Chem. Eng.* **2019**, *23*, 106–114.

(28) Chen, L.; Pilania, G.; Batra, R.; Huan, T. D.; Kim, C.; Kuenneth, C.; Ramprasad, R. Polymer Informatics: Current Status and Critical next Steps. *Mater. Sci. Eng. R Reports* **2021**, *144*, 100595.

(29) Chan, D.; Chien, J.-C.; Axpe, E.; Blankemeier, L.; Baker, S. W.; Swaminathan, S.; Piunova, V. A.; Zubarev, D. Y.; Soh, H. T.; Appel, E. A. Combinatorial Polyacrylamide Hydrogels for Preventing Biofouling on Implantable Biosensors. *bioRxiv* **2020**, 2020.05.25.115675.

(30) Kumar, R.; Le, N.; Tan, Z.; Brown, M. E.; Jiang, S.; Reineke, T. M. Efficient Polymer-Mediated Delivery of Gene-Editing Ribonucleoprotein Payloads through Combinatorial Design, Parallelized Experimentation, and Machine Learning. *ACS Nano* **2020**, *14* (12), 17626-17639.

(31) Doan Tran, H.; Kim, C.; Chen, L.; Chandrasekaran, A.; Batra, R.; Venkatram, S.; Kamal, D.; Lightstone, J. P.; Gurnani, R.; Shetty, P.; et al. Machine-Learning Predictions of Polymer Properties with Polymer Genome. *J. Appl. Phys.* **2020**, *128* (17).

(32) Lin, T. S.; Coley, C. W.; Mochigase, H.; Beech, H. K.; Wang, W.; Wang, Z.; Woods, E.; Craig, S. L.; Johnson, J. A.; Kalow, J. A.; et al. BigSMILES: A Structurally-Based Line Notation for Describing Macromolecules. *ACS Cent. Sci.* **2019**, *5* (9), 1523–1531.

(33) Lin, T. S.; Rebello, N. J.; Beech, H. K.; Wang, Z.; El-Zaatari, B.; Lundberg, D. J.; Johnson, J. A.; Kalow, J. A.; Craig, S. L.; Olsen, B. D. PolyDAT: A Generic Data Schema for Polymer Characterization. *J. Chem. Inf. Model.* **2021**, *61*, 1150-1163.

(34) Kim, C.; Chandrasekaran, A.; Jha, A.; Ramprasad, R. Active-Learning and Materials Design: The Example of High Glass Transition Temperature Polymers. *MRS Commun.* **2019**, *9* (3), 860–866.

(35) Zhang, Y.; Xu, X. Machine Learning Glass Transition Temperature of Polyacrylamides Using Quantum Chemical Descriptors. *Polym. Chem.* **2021**, *12* (6), 843–851.

(36) Pilania, G.; Iverson, C. N.; Lookman, T.; Marrone, B. L. Machine-Learning-Based Predictive Modeling of Glass Transition Temperatures: A Case of Polyhydroxyalkanoate Homopolymers and Copolymers. *J. Chem. Inf. Model.* **2019**, *59* (12), 5013–5025.

(37) Park, N. H.; Zubarev, D. Y.; Hedrick, J. L.; Kiyek, V.; Corbet, C.; Lottier, S. A Recommender System for Inverse Design of Polycarbonates and Polyesters.

*Macromolecules* **2020**, *53* (24), 10847–10854.

(38) Wu, S.; Kondo, Y.; Kakimoto, M. aki; Yang, B.; Yamada, H.; Kuwajima, I.; Lambard, G.; Hongo, K.; Xu, Y.; Shiomi, J.; et al. Machine-Learning-Assisted Discovery of Polymers with High Thermal Conductivity Using a Molecular Design Algorithm. *NPJ Comput. Mater.* **2019**, *5* (1).

(39) Kholodovych, V.; Gubskaya, A. V.; Bohrer, M.; Harris, N.; Knight, D.; Kohn, J.; Welsh, W. J. Prediction of Biological Response for Large Combinatorial Libraries of Biodegradable Polymers: Polymethacrylates as a Test Case. *Polymer.* **2008**, *49* (10), 2435–2439.

(40) Pruksawan, S.; Lambard, G.; Samitsu, S.; Sodeyama, K.; Naito, M. Prediction and Optimization of Epoxy Adhesive Strength from a Small Dataset through Active Learning. *Sci. Technol. Adv. Mater.* **2019**, *20* (1), 1010–1021.

(41) Srinivas, M.; Morel, P. A.; Ernst, L. A.; Laidlaw, D. H.; Ahrens, E. T. Fluorine-19 MRI for Visualization and Quantification of Cell Migration in a Diabetes Model. *Magn. Reson. Med.* **2007**, *58* (4), 725–734.

(42) Janjic, J. M.; Ahrens, E. T. Fluorine-Containing Nanoemulsions for MRI Cell Tracking. *WIREs Nanomed Nanobiol.* **2009**, *1*, 492–501.

(43) Srinivas, M.; Heerschap, A.; Ahrens, E. T.; Figdor, C. G.; de Vries, I. J. M. 19F MRI for Quantitative in Vivo Cell Tracking. *Trends Biotechnol.* **2010**, *28* (7), 363–370.

(44) Chapelin, F.; Capitini, C. M.; Ahrens, E. T. Fluorine-19 MRI for Detection and Quantification of Immune Cell Therapy for Cancer. *J. Immunother. Cancer* **2018**, *6* (1).

(45) Taylor, N. G.; Chung, S. H.; Kwansa, A. L.; Johnson, R. R.; Teator, A. J.; Milliken, N. J. B.; Koshlap, K. M.; Yingling, Y. G.; Lee, Y. Z.; Leibfarth, F. A. Partially Fluorinated

Copolymers as Oxygen Sensitive 19F MRI Agents. *Chem. Eur. J.* **2020**, *26* (44), 9982–9990.

(46) Tirotta, I.; Dichiarante, V.; Pigliacelli, C.; Cavallo, G.; Terraneo, G.; Bombelli, F. B.; Metrangolo, P.; Resnati, G. 19F Magnetic Resonance Imaging (MRI): From Design of Materials to Clinical Applications. *Chem. Rev.* **2015**, *115* (2), 1106–1129.

(47) Gopakumar, A. M.; Balachandran, P. V.; Xue, D.; Gubernatis, J. E.; Lookman, T. Multi-Objective Optimization for Materials Discovery via Adaptive Design. *Sci. Rep.* **2018**, *8* (1), 1–12.

(48) Settles, B. *From Theories to Queries: Active Learning in Practice*. Guyon, I; Cawley, G.; Dror, G.; Lemaire, V.; Statnikov, A., Eds.; JMLR Workshop & Conference Proceedings: Sardinia, Italy, 2011.

(49) *Automated Machine Learning: Methods, Systems, and Challenges*; Hutter, F., Vanschoren, J., Kotthoff, L., Eds.; Springer: Cham, Switzerland, 2019.

(50) Feurer, M.; Eggensperger, K.; Falkner, S.; Lindauer, M.; Hutter, F. Auto-Sklearn 2.0: The Next Generation. *arXiv* **2020**, arXiv:2007.04074.

(51) Olson, R. S.; Bartley, N.; Urbanowicz, R. J.; Moore, J. H. Evaluation of a Tree-Based Pipeline Optimization Tool for Automating Data Science. In *Proceedings of the Genetic and Evolutionary Computation Conference 2016*; GECCO '16; Association for Computing Machinery: New York, NY, USA, 2016; pp 485–492.

(52) Pedregosa, F.; Varoquaux, G.; Gramfort, A.; Michel, V.; Thirion, B.; Grisel, O.; Blondel, M.; Prettenhofer, P.; Weiss, R.; Dubourg, V.; et al. Scikit-Learn: Machine Learning in Python. *J. Mach. Learn. Res.* **2011**, *12*, 2825–2830.

(53) Chen, T.; Guestrin, C. XGBoost: A Scalable Tree Boosting System. In *Proceedings of the*

*22nd ACM SIGKDD International Conference on Knowledge Discovery and Data Mining*; KDD '16; Association for Computing Machinery: New York, NY, USA, 2016; pp 785–794.

(54) Duan, T.; Avati, A.; Ding, D. Y.; Basu, S.; Ng, A. Y.; Schuler, A. NGBoost: Natural Gradient Boosting for Probabilistic Prediction. *arXiv* **2019**, arXiv:1910.03225.

(55) Reis, M. H.; Leibfarth, F. A.; Pitet, L. M. Polymerizations in Continuous Flow: Recent Advances in the Synthesis of Diverse Polymeric Materials. *ACS Macro Lett.* **2020**, *9* (1), 123–133.

(56) Zhou, Y.; Gu, Y.; Jiang, K.; Chen, M. Droplet-Flow Photopolymerization Aided by Computer: Overcoming the Challenges of Viscosity and Facilitating the Generation of Copolymer Libraries. *Macromolecules* **2019**, *52* (15), 5611–5617.

(57) Reis, M. H.; Davidson, C. L. G.; Leibfarth, F. A. Continuous-Flow Chemistry for the Determination of Comonomer Reactivity Ratios. *Polym. Chem.* **2018**, *9* (13), 1728–1734.

(58) Tonhauser, C.; Natalello, A.; Löwe, H.; Frey, H. Microflow Technology in Polymer Synthesis. *Macromolecules* **2012**, *45* (24), 9551–9570.

(59) Walsh, D. J.; Schinski, D. A.; Schneider, R. A.; Guironnet, D. General Route to Design Polymer Molecular Weight Distributions through Flow Chemistry. *Nat. Commun.* **2020**, *11* (1), 3094.

(60) Rubens, M.; Vrijsen, J. H.; Laun, J.; Junkers, T. Precise Polymer Synthesis by Autonomous Self-Optimizing Flow Reactors. *Angew. Chemie* **2019**, *131* (10), 3215–3219.

(61) Reis, M. H.; Varner, T. P.; Leibfarth, F. A. The Influence of Residence Time Distribution on Continuous-Flow Polymerization. *Macromolecules* **2019**, *52* (9), 3551–3557.

(62) Lu, S.; Wang, K. Kinetic Study of TBD Catalyzed δ-Valerolactone Polymerization Using

a Gas-Driven Droplet Flow Reactor. *React. Chem. Eng.* **2019**, *4* (7), 1189–1194.

(63) Lin, B.; Hedrick, J. L.; Park, N. H.; Waymouth, R. M. Programmable High-Throughput Platform for the Rapid and Scalable Synthesis of Polyester and Polycarbonate Libraries. *J. Am. Chem. Soc.* **2019**, *141* (22), 8921–8927.

(64) Wang, K.; Peng, H.; Thurecht, K. J.; Puttick, S.; Whittaker, A. K. Segmented Highly Branched Copolymers: Rationally Designed Macromolecules for Improved and Tunable 19F MRI. *Biomacromolecules* **2015**, *16* (9), 2827–2839.

(65) Reizman, B. J.; Jensen, K. F. Simultaneous Solvent Screening and Reaction Optimization in Microliter Slugs. *Chem. Commun.* **2015**, *51* (68), 13290–13293.

(66) Sohrabi, S.; Kassir, N.; Keshavarz Moraveji, M. Droplet Microfluidics: Fundamentals and Its Advanced Applications. *RSC Adv.* **2020**, *10* (46), 27560–27574.

(67) Li, M.; Zhang, Y.; Zhang, J.; Peng, M.; Yan, L.; Tang, Z.; Wu, Q. Continuous Gas–Liquid–Solid Slug Flow for Sustainable Heterogeneously Catalyzed PET-RAFT Polymerization. *Ind. Eng. Chem. Res.* **2021**, *60*, 5451-5462.

(68) Ardana, A.; Whittaker, A. K.; Thurecht, K. J. PEG-Based Hyperbranched Polymer Theranostics: Optimizing Chemistries for Improved Bioconjugation. *Macromolecules* **2014**, *47* (15), 5211–5219.

(69) Zhao, W.; Ta, H. T.; Zhang, C.; Whittaker, A. K. Polymerization-Induced Self-Assembly (PISA) - Control over the Morphology of 19F-Containing Polymeric Nano-Objects for Cell Uptake and Tracking. *Biomacromolecules* **2017**, *18* (4), 1145–1156.

(70) Wang, K.; Peng, H.; Thurecht, K. J.; Puttick, S.; Whittaker, A. K. Multifunctional Hyperbranched Polymers for CT/ 19 F MRI Bimodal Molecular Imaging. *Polym. Chem.* **2016**, *7* (5), 1059–1069.

(71) Zhang, C.; Moonshi, S. S.; Peng, H.; Puttick, S.; Reid, J.; Bernardi, S.; Searles, D. J.; Whittaker, A. K. Ion-Responsive 19 F MRI Contrast Agents for the Detection of Cancer Cells. *ACS Sensors* **2016**, *1* (6), 757–765.

(72) Wang, K.; Peng, H.; Thurecht, K. J.; Whittaker, A. K. Fluorinated POSS-Star Polymers for 19 F MRI. *Macromol. Chem. Phys.* **2016**, *217* (20), 2262–2274.

(73) Wang, K.; Peng, H.; Thurecht, K. J.; Puttick, S.; Whittaker, A. K. PH-Responsive Star Polymer Nanoparticles: Potential 19F MRI Contrast Agents for Tumour-Selective Imaging. *Polym. Chem.* **2013**, *4* (16), 4480–4489.

(74) Zhang, C.; Moonshi, S. S.; Han, Y.; Puttick, S.; Peng, H.; Magoling, B. J. A.; Reid, J. C.; Bernardi, S.; Searles, D. J.; Král, P.; et al. PFPE-Based Polymeric 19F MRI Agents: A New Class of Contrast Agents with Outstanding Sensitivity. *Macromolecules* **2017**, *50* (15), 5953–5963.

(75) Munkhbat, O.; Canakci, M.; Zheng, S.; Hu, W.; Osborne, B.; Bogdanov, A. A.; Thayumanavan, S. 19 F MRI of Polymer Nanogels Aided by Improved Segmental Mobility of Embedded Fluorine Moieties. *Biomacromolecules* **2019**, *20* (2), 790–800.

(76) Thurecht, K. J.; Blakey, I.; Peng, H.; Squires, O.; Hsu, S.; Alexander, C.; Whittaker, A. K. Functional Hyperbranched Polymers: Toward Targeted in Vivo 19F Magnetic Resonance Imaging Using Designed Macromolecules. *J. Am. Chem. Soc.* **2010**, *132* (15), 5336–5337.

(77) Fu, C.; Zhang, C.; Peng, H.; Han, F.; Baker, C.; Wu, Y.; Ta, H.; Whittaker, A. K. Enhanced Performance of Polymeric 19F MRI Contrast Agents through Incorporation of Highly Water-Soluble Monomer MSEA. *Macromolecules* **2018**, *51* (15), 5875–5882.

(78) Bagheri, A.; Bainbridge, C. W. A.; Engel, K. E.; Qiao, G. G.; Xu, J.; Boyer, C.; Jin, J. Oxygen Tolerant PET-RAFT Facilitated 3D Printing of Polymeric Materials under Visible

LEDs. *ACS Appl. Polym. Mater.* **2020**, *2* (2), 782–790.

(79) Song, Y.; Kim, Y.; Noh, Y.; Singh, V. K.; Behera, S. K.; Abudulimu, A.; Chung, K.; Wannemacher, R.; Gierschner, J.; Lüer, L.; et al. Organic Photocatalyst for Ppm-Level Visible-Light-Driven Reversible Addition–Fragmentation Chain-Transfer (RAFT) Polymerization with Excellent Oxygen Tolerance. *Macromolecules* **2019**, *52* (15), 5538–5545.

(80) Szymański, J. K.; Pérez-Mercader, J. Direct Optical Observations of Vesicular Self-Assembly in Large-Scale Polymeric Structures during Photocontrolled Biphasic Polymerization. *Polym. Chem.* **2016**, *7* (47), 7211–7215.

(81) Albertsen, A. N.; Szymański, J. K.; Pérez-Mercader, J. Emergent Properties of Giant Vesicles Formed by a Polymerization-Induced Self-Assembly (PISA) Reaction. *Sci. Rep.* **2017**, *7* (1), 41534.

(82) Ren, K.; Perez-Mercader, J. Thermoresponsive Gels Directly Obtained via Visible Light-Mediated Polymerization-Induced Self-Assembly with Oxygen Tolerance. *Polym. Chem.* **2017**, *8* (23), 3548–3552.

(83) Niu, J.; Page, Z. A.; Dolinski, N. D.; Anastasaki, A.; Hsueh, A. T.; Soh, H. T.; Hawker, C. J. Rapid Visible Light-Mediated Controlled Aqueous Polymerization with In Situ Monitoring. *ACS Macro Lett.* **2017**, *6* (10), 1109–1113.

(84) Xu, J.; Jung, K.; Boyer, C. Oxygen Tolerance Study of Photoinduced Electron Transfer–Reversible Addition–Fragmentation Chain Transfer (PET-RAFT) Polymerization Mediated by Ru(Bpy) 3 Cl 2. *Macromolecules* **2014**, *47* (13), 4217–4229.

(85) Shanmugam, S.; Xu, J.; Boyer, C. Photoinduced Electron Transfer–Reversible Addition–Fragmentation Chain Transfer (PET-RAFT) Polymerization of Vinyl Acetate and N -

Vinylpyrrolidinone: Kinetic and Oxygen Tolerance Study. *Macromolecules* **2014**, *47* (15), 4930–4942.

(86) Yang, P.; Pageni, P.; Kabir, M. P.; Zhu, T.; Tang, C. Metallocene-Containing Homopolymers and Heterobimetallic Block Copolymers via Photoinduced RAFT Polymerization. *ACS Macro Lett.* **2016**, *5* (11), 1293–1300.

(87) Xu, J.; Shanmugam, S.; Fu, C.; Aguey-Zinsou, K.-F.; Boyer, C. Selective Photoactivation: From a Single Unit Monomer Insertion Reaction to Controlled Polymer Architectures. *J. Am. Chem. Soc.* **2016**, *138* (9), 3094–3106.

(88) Shanmugam, S.; Xu, J.; Boyer, C. Utilizing the Electron Transfer Mechanism of Chlorophyll a under Light for Controlled Radical Polymerization. *Chem. Sci.* **2015**, *6* (2), 1341–1349.

(89) Xu, J.; Shanmugam, S.; Duong, H. T.; Boyer, C. Organo-Photocatalysts for Photoinduced Electron Transfer-Reversible Addition–Fragmentation Chain Transfer (PET-RAFT) Polymerization. *Polym. Chem.* **2015**, *6* (31), 5615–5624.

(90) Lee, I.-H.; Discekici, E. H.; Anastasaki, A.; de Alaniz, J. R.; Hawker, C. J. Controlled Radical Polymerization of Vinyl Ketones Using Visible Light. *Polym. Chem.* **2017**, *8* (21), 3351–3356.

(91) Shanmugam, S.; Xu, J.; Boyer, C. Exploiting Metalloporphyrins for Selective Living Radical Polymerization Tunable over Visible Wavelengths. *J. Am. Chem. Soc.* **2015**, *137* (28), 9174–9185.

(92) Shanmugam, S.; Xu, J.; Boyer, C. Aqueous RAFT Photopolymerization with Oxygen Tolerance. *Macromolecules* **2016**, *49* (24), 9345–9357.

(93) Shen, L.; Lu, Q.; Zhu, A.; Lv, X.; An, Z. Photocontrolled RAFT Polymerization Mediated

by a Supramolecular Catalyst. *ACS Macro Lett.* **2017**, *6* (6), 625–631.

(94) Xu, S.; Ng, G.; Xu, J.; Kuchel, R. P.; Yeow, J.; Boyer, C. 2-(Methylthio)Ethyl Methacrylate: A Versatile Monomer for Stimuli Responsiveness and Polymerization-Induced Self-Assembly in the Presence of Air. *ACS Macro Lett.* **2017**, *6* (11), 1237–1244.

(95) Ng, G.; Yeow, J.; Xu, J.; Boyer, C. Application of Oxygen Tolerant PET-RAFT to Polymerization-Induced Self-Assembly. *Polym. Chem.* **2017**, *8* (18), 2841–2851.

(96) Yeow, J.; Shanmugam, S.; Corrigan, N.; Kuchel, R. P.; Xu, J.; Boyer, C. A Polymerization-Induced Self-Assembly Approach to Nanoparticles Loaded with Singlet Oxygen Generators. *Macromolecules* **2016**, *49* (19), 7277–7285.

(97) Corrigan, N.; Almasri, A.; Taillades, W.; Xu, J.; Boyer, C. Controlling Molecular Weight Distributions through Photoinduced Flow Polymerization. *Macromolecules* **2017**, *50* (21), 8438–8448.

(98) Corrigan, N.; Rosli, D.; Jones, J. W. J.; Xu, J.; Boyer, C. Oxygen Tolerance in Living Radical Polymerization: Investigation of Mechanism and Implementation in Continuous Flow Polymerization. *Macromolecules* **2016**, *49* (18), 6779–6789.

(99) Fu, Q.; Xie, K.; McKenzie, T. G.; Qiao, G. G. Trithiocarbonates as Intrinsic Photoredox Catalysts and RAFT Agents for Oxygen Tolerant Controlled Radical Polymerization. *Polym. Chem.* **2017**, *8* (9), 1519–1526.

(100) McKenzie, T. G.; Fu, Q.; Wong, E. H. H.; Dunstan, D. E.; Qiao, G. G. Visible Light Mediated Controlled Radical Polymerization in the Absence of Exogenous Radical Sources or Catalysts. *Macromolecules* **2015**, *48* (12), 3864–3872.

(101) Quinn, J. F.; Barner, L.; Barner-Kowollik, C.; Rizzardo, E.; Davis, T. P. Reversible Addition−Fragmentation Chain Transfer Polymerization Initiated with Ultraviolet

Radiation. *Macromolecules* **2002**, *35* (20), 7620–7627.

(102) Lu, L.; Zhang, H.; Yang, N.; Cai, Y. Toward Rapid and Well-Controlled Ambient Temperature RAFT Polymerization under UV−Vis Radiation: Effect of Radiation Wave Range. *Macromolecules* **2006**, *39* (11), 3770–3776.

(103) Wang, J.; Rivero, M.; Muñoz Bonilla, A.; Sanchez-Marcos, J.; Xue, W.; Chen, G.; Zhang, W.; Zhu, X. Natural RAFT Polymerization: Recyclable-Catalyst-Aided, Opened-to-Air, and Sunlight-Photolyzed RAFT Polymerizations. *ACS Macro Lett.* **2016**, *5* (11).

(104) Bagheri, A.; Engel, K. E.; Bainbridge, C. W. A.; Xu, J.; Boyer, C.; Jin, J. 3D Printing of Polymeric Materials Based on Photo-RAFT Polymerization. *Polym. Chem.* **2020**, *11* (3), 641–647.

(105) Lamb, J. R.; Qin, K. P.; Johnson, J. A. Visible-Light-Mediated, Additive-Free, and Open-to-Air Controlled Radical Polymerization of Acrylates and Acrylamides. *Polym. Chem.* **2019**, *10* (13), 1585–1590.

(106) Kuroki, A.; Martinez-Botella, I.; Hornung, C. H.; Martin, L.; Williams, E. G. L.; Locock, K. E. S.; Hartlieb, M.; Perrier, S. Looped Flow RAFT Polymerization for Multiblock Copolymer Synthesis. *Polym. Chem.* **2017**, *8* (21), 3249–3254.

(107) Gurnani, P.; Floyd, T.; Tanaka, J.; Stubbs, C.; Lester, D.; Sanchez-Cano, C.; Perrier, S. PCR-RAFT: Rapid High Throughput Oxygen Tolerant RAFT Polymer Synthesis in a Biology Laboratory. *Polym. Chem.* **2020**, *11* (6), 1230–1236.

(108) Tanaka, J.; Gurnani, P.; Cook, A. B.; Häkkinen, S.; Zhang, J.; Yang, J.; Kerr, A.; Haddleton, D. M.; Perrier, S.; Wilson, P. Microscale Synthesis of Multiblock Copolymers Using Ultrafast RAFT Polymerisation. *Polym. Chem.* **2019**, *10* (10), 1186–1191.

(109) Parkinson, S.; Knox, S. T.; Bourne, R. A.; Warren, N. J. Rapid Production of Block

Copolymer Nano-Objects via Continuous-Flow Ultrafast RAFT Dispersion Polymerisation. *Polym. Chem.* **2020**, *11* (20), 3465–3474.

(110) Gody, G.; Barbey, R.; Danial, M.; Perrier, S. Ultrafast RAFT Polymerization: Multiblock Copolymers within Minutes. *Polym. Chem.* **2015**, *6* (9), 1502–1511.

(111) Upadhya, R.; Kanagala, M. J.; Gormley, A. J. Purifying Low-Volume Combinatorial Polymer Libraries with Gel Filtration Columns. *Macromol. Rapid Commun.* **2019**, *40* (24), 1900528.

(112) Webb, A. Increasing the Sensitivity of Magnetic Resonance Spectroscopy and Imaging. *Anal. Chem.* **2012**, *84* (1), 9–16.

(113) Butina, D. Unsupervised Data Base Clustering Based on Daylight's Fingerprint and Tanimoto Similarity: A Fast and Automated Way To Cluster Small and Large Data Sets. *J. Chem. Inf. Comput. Sci.* **1999**, *39* (4), 747–750.

(114) McInnes, L.; Healy, J.; Melville, J. UMAP: Uniform Manifold Approximation and Projection for Dimension Reduction. *arXiv* **2018**, arXiv:1802.03426v3.

(115) Haase, A.; Frahm, J.; Matthaei, D.; Hanicke, W.; Merboldt, K.-D. FLASH Imaging. Rapid NMR Imaging Using Low Flip-Angle Pulses. *J. Magn. Reson.* **1986**, *67* (2), 258–266.

(116) Zhang, S.; Block, K. T.; Frahm, J. Magnetic Resonance Imaging in Real Time: Advances Using Radial FLASH. *J. Magn. Reson. Imaging* **2010**, *31* (1), 101–109.

(117) Jiang, Z.-X.; Liu, X.; Jeong, E.-K.; Yu, Y. B. Symmetry-Guided Design and Fluorous Synthesis of a Stable and Rapidly Excreted Imaging Tracer for 19F MRI. *Angew. Chem. Int. Ed.* **2009**, *48* (26), 4755–4758.